Innovative Optimization of LDI-MS Porous Silicon Substrates Using Thermometer Ions

Clara Whyte Ferreira, Bastien Cabrera-Tejera, Bernard Leyh, Romain Tuyaerts, Gilles Scheen, Yannick Coffinier, Edwin De Pauw, Gauthier Eppe

Innovative Optimization of LDI-MS Porous Silicon Substrates Using Thermometer Ions

Clara Whyte Ferreira[1 2 3], Bastien Cabrera-Tejera[2], Bernard Leyh[4], Romain Tuyaerts[1], Gilles Scheen[1], Yannick Coffinier[3*], Edwin De Pauw[2*], Gauthier Eppe[2*]

1 Incize, Ottignies-Louvain-la-Neuve, Belgium

2 Mass Spectrometry Laboratory (MolSys Research Unit), University of Liège, Liège, Belgium

3 Univ. Lille, CNRS, UMR 8520 - IEMN, Lille, France

4 Molecular Dynamics Laboratory (MolSys Research Unit), University of Liège, Liège, Belgium

*Equally contributed to the paper

ABSTRACT: This study presents a methodical procedure for optimizing laser desorption/ionization mass spectrometry (LDI-MS) supports using porous silicon (PSi) substrates. The approach involves the use of substituted benzyl-pyridinium salts (thermometer ions) to obtain one metric that assesses analyte fragmentation (the effective temperature of vibration). Porous silicon substrates were synthesized via electrochemical etching of p-type silicon wafers (10-20 mΩ·cm), with etching parameters adjusted to vary porosity while maintaining a layer thickness between 700 and 1200 nm. The results revealed that PSi substrates with 40-60% porosity achieved the lowest fragmentation levels. This finding was validated through the analysis of N-Acetyl glucosamine, a carbohydrate, which confirmed the effective temperature trend. Further analysis involving peptides, specifically P14R and a peptide mix (Peptide Calibration Standard II, Bruker), demonstrated that the optimized PSi substrates enabled the desorption and ionization of peptides with a maximum mass at *m/z* 2465, corresponding to ACTH clip 1-17. These results highlight the critical role of substrate porosity in minimizing analyte fragmentation and enhancing LDI-MS performance.

In the late 1980s, Koichi Tanaka and coworkers[1] published their pioneer work in Laser Desorption Ionization Mass Spectrometry (LDI-MS). Around the same time, Karas and Hillenkamp[2], proposed a technique based on the co-crystallization of the analyte with an organic matrix that aids the desorption/ionization process and limits analyte fragmentation, the so-called Matrix-assisted laser desorption/ionization MS (MALDI-MS).

Since then, MALDI, has been established as a reliable technique for analyzing fragile non-volatile molecules within a wide range of compounds such as proteins, oligonucleotides or synthetic polymers without inducing extensive fragmentation.

Later, in the 1990s, Wei et al.[3] presented Desorption Ionization on Silicon (DIOS) hoping to overcome some of the MALDI limitations, namely:

- dependance on the quality of the matrix deposition,
- matrix interference in the mass spectra, adding background noise in the low mass range (m/z<700), and
- matrix crystal size (typically in the micrometer range) and inhomogeneity of the matrix deposition, which are limiting factors for imaging applications.

Much progress has been made in the usage of inorganic substrates in LDI-MS along with the development of distinct nanostructures made not only of silicon[4–9] but also of carbon[10], alumina[11], titania[12], germanium[13], and gold[14]. This technique holds the advantages of better resolution in the low mass range, independence on organic matrix deposition quality, multimodal capability (e.g. surface enhanced Raman spectroscopy and Fourier transform infrared spectroscopy [15]), and possibility of performing dual polarity experiments on the same substrate[12].

Although several examples of applications have been successfully demonstrated throughout the years, the mechanisms underlying LDI-MS process on those substrates is still poorly understood. Furthermore, comparing the performance of all those different substrates is not an easy task as several parameters can impact the desorption/ionization process.

Generally, LDI-MS on inorganic substrates is a harsher technique than MALDI-MS (i.e. leads to more extensive fragmentation)[16]. Therefore, to optimize and compare the substrates, one needs to quantify the degree of analyte fragmentation associated with them. Here, we propose a metric, first introduced by De Pauw et al.[17], to systematically evaluate the fragmentation of analytes across different nano substrates.

This is achieved by the characterization of the internal energy distribution of selected ions in terms of their effective temperature of vibration. The method relies on the selection of small molecular ions, such as substituted benzyl pyridinium ions having different dissociation energies, to reconstruct the internal energy distribution of the ions, P(E), which is associated to each evaluated substrate. This distribution of an ion population can then be associated with an effective temperature of vibration (T_{eff}). We can therefore compare different substrates based on this single parameter: the higher the T_{eff} of ions leaving a given substrate, the more fragmentation that substrate induces.

In this study, we compare porous silicon substrates produced by electrochemical etching of p-doped silicon wafers at different current densities. Each substrate yields a distinct value of open porosity that significantly impacts analyte fragmentation. T_{eff} values are calculated for each substrate and the obtained results are further validated by data on the fragmentation of peptides and carbohydrates samples.

MATERIALS AND METHODS

Survival yield, internal energy distributions and calculations of the effective temperatures of vibration

The internal energy distribution of the ions provides important insights into the harshness of the desorption/ionization process (e.g. fragmentation). A straightforward method for estimating this distribution consists in studying the fragmentation within a family of target ions (i.e. thermometer ions). Benzyl pyridinium (BP) salts are a good target system because they fragment by direct cleavage of the C-N bond between the substituted-benzyl radical and the pyridine moiety, as illustrated in Figure 1.

Furthermore, the use of these molecules as thermometer ions fulfils a key set of assumptions:

- Being salts, BP are already ionized in the applied solution,
- due to the large (69 to 81) number of vibrational modes, the internal energy can be considered as predominantly influenced by vibrational contributions; however the model does not account for rotational or potential vibrational-rotational coupling contributions,
- quasi-equilibrium state (the system is in a steady-state internal energy distribution, in which the energy is assumed to be statistically distributed across all vibrational modes),
- similar molecular size leading to similar number of vibrational degrees of freedom,
- simple bond cleavage mechanism associated with a loose transition state (we can neglect the reverse activation barrier, so that the dissociation threshold energy can be equated to the dissociation energy).

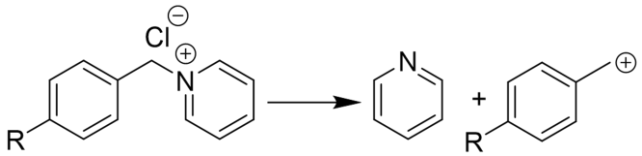

Figure 1 – Schematic fragmentation mechanism of substituted Benzyl Pyridinium salts by the cleavage of the C-N bond

By changing the substituent, the energy required to fragment the ions (i.e. dissociation energy E_0) can be tuned. Thus, the internal energy distribution can be reconstructed by sweeping through these different energies (i.e. changing the BP analyte) and calculating the obtained survival yield (SY) for each mass spectrum, such as:

$$SY = \frac{I_P}{I_P + I_F} \qquad (1)$$

where I_P is the parent ion intensity and I_F is the charged fragment ion intensity. The SY values are then plotted as a function of E_0 and a fitting procedure is applied to extract the parameters of the resulting S-shaped curve.

This S-shaped curve represents the integral of the $P(E)$ function, which describes the internal energy distribution. Assuming a Boltzmann distribution, P(E) can be expressed as:

$$P(E) = AE^{s'-1}e^{\frac{-E}{k_B T}} \qquad (2)$$

Where A is a normalization factor, E is the energy level where the distribution is evaluated, s' corresponds to the effective number of normal vibrational modes (considering temperature effects on their excitation), k_B is the Boltzmann constant, and T is the temperature that describes this distribution.

The S-shaped curve can then be obtained from:

$$F(E) = \int_0^E P(E)dE = \frac{\gamma(s', \frac{E}{k_B T})}{\Gamma(s')} \qquad (3)$$

Where $\gamma(s', \frac{E}{k_B T})$ is the lower incomplete gamma function and $\Gamma(s')$ is the gamma function.

For each thermometer ion, the S-shaped curve is fitted using equation (3). The final effective temperature of vibration (T_{eff}) is then determined by averaging the temperatures obtained from the fits across different thermometer ions.

The T_{eff} associated with the internal energy distributions are directly linked to the fragmentation of the analytes: higher T_{eff} values lead to increased fragmentation. An analogy can be drawn with ions in thermal equilibrium within a hot gas bath. In this analogy, T_{eff} represents the

temperature at which the ions would fragment similarly to what is observed during the mass spectrometry experiment.

Furthermore, by calculating the mean energy value from the obtained Boltzmann distribution, it is possible to estimate a commonly used parameter in the literature: the average internal energy of the ions, $\overline{E}_{int}$, given by:

$$\overline{E}_{int} = \frac{\int_0^\infty E\,P(E)dE}{\int_0^\infty P(E)dE} = s' k_B T \qquad (4)$$

This is a brief overview of the fitting procedure. For a more detailed explanation, analytical development and the complete methodology, please refer to the Supporting Information. Further theoretical background and internal energy distribution discussion can be found in a special feature tutorial by Vékey[18].

The fitting procedures were performed using an in-house Python script. The E_0 and $\tilde{\nu}_i$ (wave number of each normal mode of the ions) for each thermometer ion were obtained from density functional theory (DFT) simulations [B3LYP 6-311G++(d,p)] using Gaussian 16, Revision B.01[19].

Porous silicon substrates fabrication and characterization

Boron-doped silicon wafers (<100> crystalline orientation, 10-20 mΩ.cm) were electrochemically etched in a 3:3:4 HF(49%): isopropyl alcohol:H_2O electrolyte, and rinsed in isopropyl alcohol (IPA). To stabilize the surfaces, a 1 hour oxidation at 350°C under air was performed. Current densities and porosification times were tuned, with the aid of a Keithley 2460 SourceMeter (Keithley Instruments) to yield the largest possible range of porosities and layer thicknesses of 1 µm.

The thickness and the porosity of the PSi layers were characterized from reflective spectra obtained using a fiber-coupled Ocean Optics JAZ spectrometer and a 10-mW halogen light source. The data were fitted using the spectroscopic liquid infiltration method (SLIM)[20], before and after oxidation, and thickness values were confirmed by scanning-electron microscopy (SEM) using a Zeiss Auriga FIB-SEM (Carl Zeiss Microscopy) .

To allow the deposition of aqueous solutions on localized spots a hydrophobic surrounding is needed. Thus, the PSi substrates were, first, subjected to a 15 min UV-ozone treatment (to expose the hydroxyl groups on the surface). Then a solution was prepared with 25 mL of 70:30 hexane: dichloromethane (DCM) and 25 µL of octadecyl trichlorosilane (OTS). The PSi substrates were then immersed in this solution for 1 hour and rinsed with DCM and IPA. The application spots were obtained by local degradation of the grafted hydrophobic monolayer with the aid of a patterned chromium/quartz mask under UV-ozone for 30 minutes.

A bare silicon wafer, bearing only the native oxide, was also subjected to the OTS functionalization and degradation of selected zones for analyte application to allow comparative mass spectrometry experiments.

Analytes preparation

Benzyl pyridinium salts synthesis protocol is described elsewhere[17]. Here, BP salts substituted in the para (p), and meta (m) positions were selected, namely: pCH_3, mCH_3, pCN and $pOCH_3$. Solutions were prepared to yield 10^{-4} M concentration in water.

α-cyano-4-hydroxycinnamic acid (CHCA) (Sigma-Aldrich) and 2,5-dihydroxybenzoic acid (DHB) (Sigma-Aldrich) MALDI matrices solutions were prepared in water by dissolving 20 mg of CHCA in 2 mL of water and 50 mg of DHB in 2 mL of water.

Two peptide calibration standards were used in this study: the Peptide Calibration Standard II (Ref: 8222570, Bruker, Germany) and the ProteoMassTMP14R MALDI-MS Standard ($[M+H]^+$ monoisotopic mass = 1533.8582 Da) (Ref: P2613-1VL, Sigma-Aldrich, Belgium). Samples were prepared to obtain solution concentrations of 10 µM for each peptide in water.

N-acetyl-D-glucosamine (221.0 Da) (Merck) was used as reference carbohydrate in this study. It was dissolved in water to obtain 10^{-2} M solutions.

For every analysis, a volume of 0.5 µL of analyte was deposited on 1 mm diameter spots patterned on the different substrates.

LDI-MS analysis

All experiments were performed using a rapifleX instrument (Bruker Daltonics). A smartbeam 3D pulsed Nd:YAG laser at a wavelength of 355 nm was operated at 5kHz and the number of shots was fixed at 1000. Laser power percentage (laser offset at 15%, and range 30%) were varied from 20 to 45%.

The obtained data was analyzed using an in-house Python script (pyOpenMS library)[21].

RESULTS AND DISCUSSION

Porous silicon (PSi) substrates possess various morphological features, such as porosity, pore size, pore morphology, layer thickness, and surface chemistry. Each of these properties can influence the laser desorption/ionization (LDI) process, although the exact extent of their impact needs to be determined.

In this study, we focused on characterizing the morphological properties of PSi, with particular emphasis on the influence of porosity, while keeping other parameters constant. By using thermometer ions and analyzing small metabolites, we aim to explore potential correlations between surface morphology and LDI-MS performance, particularly in terms of analyte fragmentation.

Fabrication and characterization of PSi

Electrochemical etching of silicon with current densities between 20 and 100 mA/cm^2 resulted in PSi samples with open porosities ranging from 27 to 71 % (characterized by spectroscopic liquid infiltration method [20]).

As an example, Figure 2 shows a porous silicon surface after OTS grafting and patterning (for droplet confinement) and SEM images. Cross sections showed thicknesses ranging from 0.7 to 1.2 µm. From top view and cross sec-

tion image inspection, the average pore size is estimated between 8 and 20 nm.

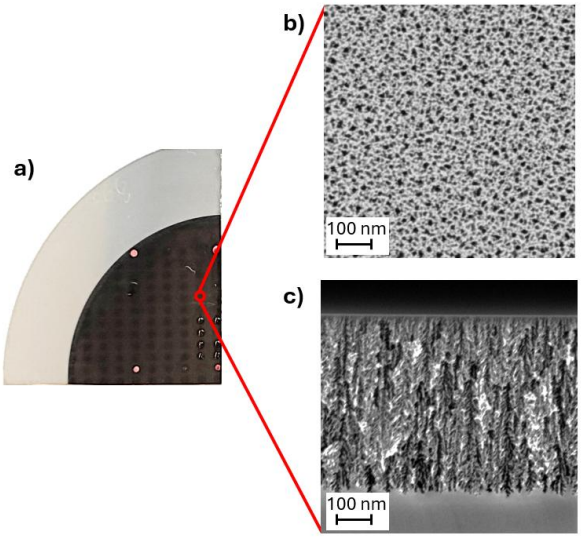

Figure 2 – Porous silicon images: a) porosified silicon wafer after hydrophobic patterning for droplet confinement; scanning electron microscopy images of a freshly etched porous silicon surface in b) top view and c) cross section.

A summary of the results is shown in Table 1. In the SLIM model, the thickness values are fixed from the SEM measurements prior to the porosity calculations. Although the oxidation of the porous silicon changed the refractive index of the skeleton, no significant changes in the porosity were observed.

Table 1 – Thickness (from scanning electron microscopy) and porosity (from spectroscopic liquid infiltration) values for the fabricated porous silicon (PSi) samples. Each value represents the average of three measurements on the same sample, with error values indicating the standard deviation across those measurements.

Porous silicon surface	Thickness (μm)	Freshly-etched sample porosity (%)	Oxidized sample porosity (%)
PSi1	0.870	26.7 ± 1.6	29.0 ± 2.1
PSi2	1.091	39.5 ± 0.9	31.3 ± 0.7
PSi3	1.226	42.5 ± 0.3	34.0 ± 2.9
PSi4	1.222	51.6 ± 3.5	44.8 ± 3.0
PSi5	1.156	52.1 ± 0.8	45.6 ± 3.1
PSi6	0.715	46.6 ± 2.3	47.7 ± 2.1
PSi7	1.029	52.6 ± 1.1	49.0 ± 0.4
PSi8	1.128	59.2 ± 2.3	56.9 ± 1.6
PSi9	0.782	70.5 ± 2.1	70.3 ± 2.0

Survival yield, effective temperature of vibration and internal energy calculations

The dissociation energy (E_0) values obtained from the DFT computations are provided in Table 2. More computational details and results are available in the supporting information.

The calculated E_0 values demonstrate a consistent trend with previous literature reports, though they are slightly higher, which can be attributed to the use of a larger and more precise basis set[22].

The thermometer ions selected were chosen due to their distinct E_0 values that allow scanning the energy through a large range. Since all the thermometer ions are analyzed using the same instrument, the "kinetic shift" effect has been neglected.

Table 2 – Dissociation energies (E_0) obtained from DFT computations [B3LYP 6-311G++(d,p)] for substituted benzyl pyridinium salts

Substituent	E_0 (eV)
p-OCH_3	1.580
p-CH_3	1.950
m-CH_3	2.134
p-CN	2.428

The SY vs E_0 plots are shown in Figure 3. The survival yields of each molecule are calculated from the relative intensities of the mass spectra and plotted as a function of the dissociation energy. Furthermore, two points are added manually at $E_0 = 0$ eV and $E_0 = 5$ eV with respective survival yields of 0 and 1 to account for the extreme cases (only fragments observed, and no fragments observed, respectively). The data points are then fitted using the F(E) expression, as described in Equation (3), obtained from a Boltzmann distribution P(E). The derivative of these functions lead to the P(E) distribution, Equation (2) as shown in Figure 4.

The effective temperatures can be obtained from the fitting procedure using the F(E) function, equation (3). The results are shown in Table 3. More details on the error propagation throughout different fitting and calculation steps are available in the supporting information.

When plotting these values as a function of the PSi sample porosity in Figure 5, one can see a clear tendency with a quadratic behavior: low porosity values (20 – 30%) lead to high T_{eff} values (extensive fragmentation) while the lowest T_{eff} values are obtained for porosities between 40 and 55%, followed by an increase when 70% porosity is approached.

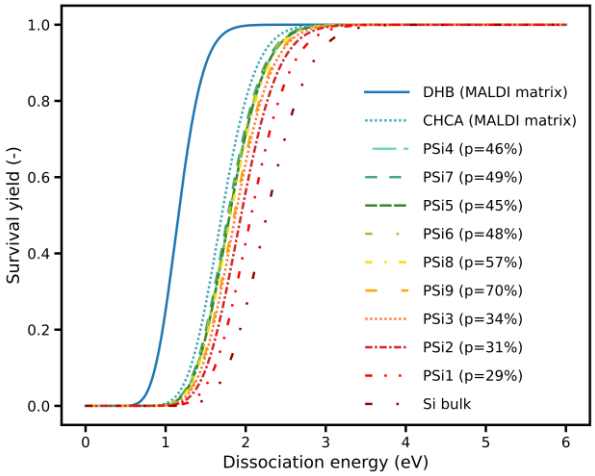

Figure 3 - Survival yield (SY) as a function of dissociation energy for bulk silicon, selected MALDI matrices, and oxidized porous silicon (PSi) with different porosities. SY values are from mass spectra, and dissociation energies from DFT computations. The curves represent the fitted F(E) (integral of the Boltzmann distribution P(E)). Data points are omitted for clarity but available in the supporting information.

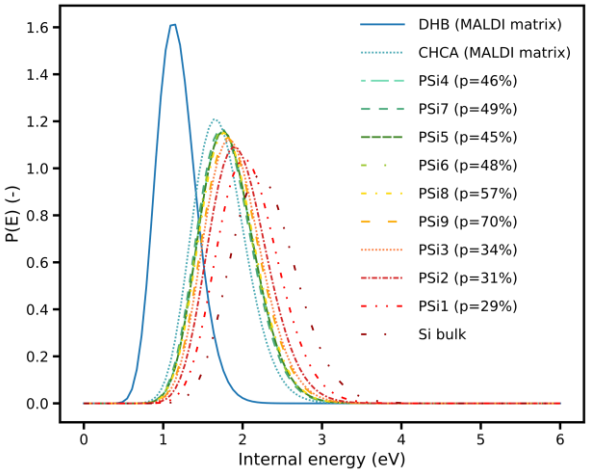

Figure 4 – Internal energy distributions: Boltzmann distributions described by T_{eff} (effective temperature of vibration).

Table 3 – Effective temperature values for the different substrates and matrices tested.

Substrate/Matrix	T_{eff} (K)	$\overline{E}_{int}$
PSi1 (p=29%)	841 ± 3	2.091 ± 0.006
PSi2 (p=31%)	813 ± 1	1.965 ± 0.002
PSi3 (p=34%)	797 ± 1	1.894 ± 0.002
PSi4 (p=45%)	780 ± 2	1.821 ± 0.005
PSi5 (p=46%)	779 ± 1	1.818 ± 0.002
PSi6 (p=48%)	778 ± 2	1.812 ± 0.005
PSi7 (p=49%)	775 ± 3	1.798 ± 0.006
PSi8 (p=57%)	783 ± 1	1.834 ± 0.002
PSi9 (p=70%)	793 ± 2	1.877 ± 0.005
Bulk silicon (Si)	884 ± 3	2.287 ± 0.008
CHCA (MALDI matrix)	756 ± 3	1.721 ± 0.007
DHB (MALDI matrix)	620 ± 1	1.177 ± 0.002

Furthermore, the effective temperature of the ions when using two MALDI matrices (CHCA and DHB), and a bulk silicon surface were determined. The LDI-MS on porous silicon is a harsher process (T_{eff} (PSi)=775 - 841 K) than MALDI-MS (T_{eff} (CHCA)=756 K and T_{eff} (DHB)=620 K) but the presence of the porous nanostructure contributes to a lower fragmentation when compared to a bulk silicon surface (T_{eff} (Si)=884 K). Those results suggest that the indirect energy transfer to the analytes, that is first absorbed by the porous silicon, protects the analyte and leads to decreased fragmentation.

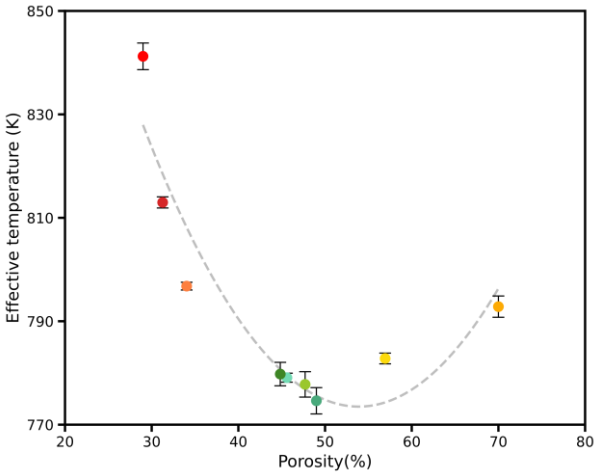

Figure 5 - Effective temperature as a function of porosity for approximately 1µm thick porous silicon substrates.

While these results indicate that the porous silicon nanostructure mitigates analyte fragmentation through indirect energy transfer, several other factors may influence the desorption/ionization process. These include the interaction forces between the analyte and the surface, the possibility of analyte crystallization within the nanostructure[23] and properties that vary with porosity such as absorption of laser irradiation[24], thermal conductivity, and heat capacity [25] . Although these parameters were not fully investigated in this study due to limitations in available experimental tools, further research employing more advanced techniques will be required to comprehensively characterize their effects.

Small metabolite analysis

Studying thermometer ions provides valuable insights into the fragmentation of analytes and the desorption process. However, since those molecules are already charged, we gained little information on the ionization process.

To better understand the effect of porous silicon morphology on the combined desorption/ionization process, N-acetyl glucosamine (GlcNAc, 221.0 Da) was deposited on the PSi surfaces and the obtained LDI-MS spectra were analyzed. This molecule is comparable to thermometer ions in terms of number of vibrational degrees of freedom (3N-6 =84), making it a good model to validate if the observed fragmentation tendency with porosity still holds in the case of initially non-ionized molecules.

As shown in

Figure 6, the intact molecule is mainly detected in the form of its sodium adduct $[M + Na]^+$ (m/z = 244.1). The observed fragments are $[M - C_2H_4NO + Na]^+$ (m/z = 186.2), and $[M - C_2H_4NO - H_2O + Na]^+$ (m/z = 168.0). We can see higher fragmentation for the two extreme porosity values (29 and 70%) when compared to the porosity presenting the lowest T_{eff} values (48-49%), confirming what was previously observed with the thermometer ions. Moreover, the similarity between the spectra for the 48% and 49% porosity samples demonstrates the reproducibility of the fragmentation behavior.

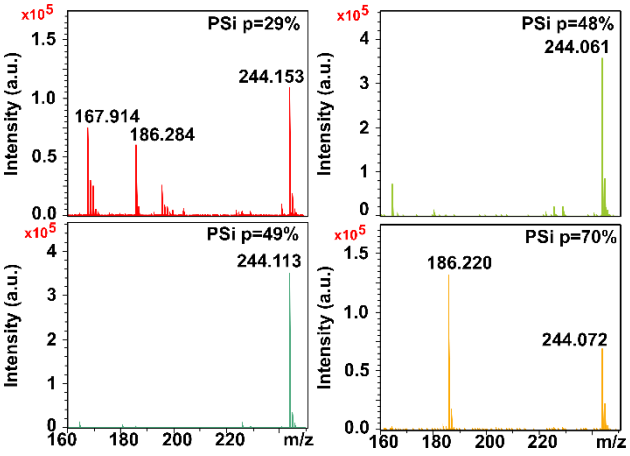

Figure 6 - Mass spectra of N-acetyl glucosamine obtained from porous silicon surfaces (PSi) with different porosities (p). The observed peaks correspond to the sodium adduct of the intact molecule $[M+Na]^+$ (m/z = 244.1), and the fragments $[M-C_2H_4NO+Na]^+$ (m/z = 186.2), and $[M-C_2H_4NO-H_2O+Na]^+$ (m/z = 168.0). Less fragmentation is observed for PSi with 48 and 49% porosities which have lower effective temperature values compared to the fragmenting surfaces (PSi p=29% and 70%).

To go further and look at fragmentation using a small metabolite, a model peptide called P14R, composed of 14 prolines and one arginine was analyzed. The identified fragments follow the nomenclature schematically shown in Figure 7 for a model peptide.

By examining P14R fragments, in Figure 7 (logarithmic scale), the fragmentation tendency is evidenced once again when comparing surfaces leading to high ion T_{eff} (with a porosity of 31%), with surfaces leading to lower ion T_{eff} (with a porosity of 45%), and on a MALDI matrix (CHCA).

On the porous silicon substrates, although the precursor ion was detected in diverse forms ($[M+H]^+$, $[M+Na]^+$, $[M+K]^+$), fragments were only detected as $[M+H]^+$ ions.

We observe both *a* and *y* fragment types on the PSi surfaces, corresponding to the sequential loss of prolines. *a*-type fragments are typically associated with thermal fragmentation pathways[26], while *y*-type fragments may indicate either a radical-based or a thermal mechanism[27]. To clarify the exact fragmentation pathway, further experiments are underway using instruments with improved mass accuracy and resolution. It is also noteworthy that these findings may not apply universally to all LDI-MS substrates, and additional research is ongoing to fully elucidate the underlying fragmentation mechanisms.

Finally, to test the limits of the substrates and verify what is the highest peptide mass that can be efficiently desorbed/ionized, we analyzed a peptide standard mixture (Peptide Calibration Standard II) composed of the peptides

listed in Table 4. The LDI-MS analysis, shown in Figure 9, shows the desorption/ionization up to *m/z* 2465.42 (ACTH clip 18-39). No correlation could be established between the peptides' isoelectric point and their desorption/ionization intensity.

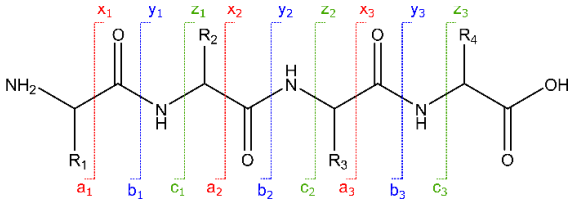

Figure 7 - Schematic representation of a peptide fragmentation and the nomenclature of the fragments.

Table 4 – Masses of peptides composing the Peptide Calibration Standard II.

Peptide	$[M+H]^+$ monoisotopic mass	Isoelectric point
Bradykinin 1-7 (P1)	757.3992	10.47
Angiotensin II (P2)	1046.5418	7.37
Angiotensin I (P3)	1296.6848	7.52
Substance (P4)	1347.7354	10.61
Bombesin (P5)	1619.8223	7.38
ACTH clip 1-17 (P6)	2093.0862	10.24
ACTH clip 18-39 (P7)	2465.1983	4.41
Somatostatin 28 (P8)	3147.4719	9.09

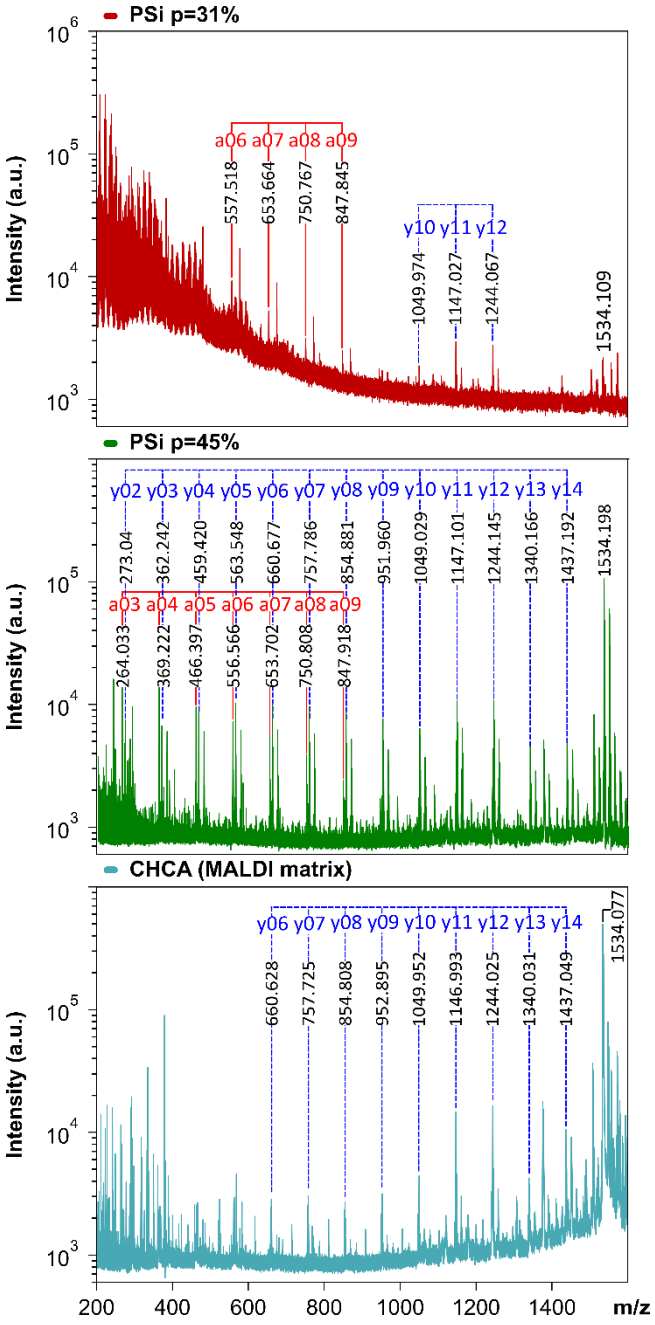

Figure 8- Mass spectra for the P14 peptide (14 prolines and 1 arginine) in logarithmic scale for better visualization. From top to bottom, the spectra were obtained on: (1) low porosity (p) PSi surface (p=31%) exhibiting a high effective temperature value (813 K), (2) intermediate porosity PSi surface (p=45%) exhibiting a lower effective temperature value (780 K) and a MALDI matrix (CHCA) that has the lowest effective temperature (756 K) amongst the three. The observed fragments are mainly of type *y* but an *a* series is also observed on PSi p=45%.

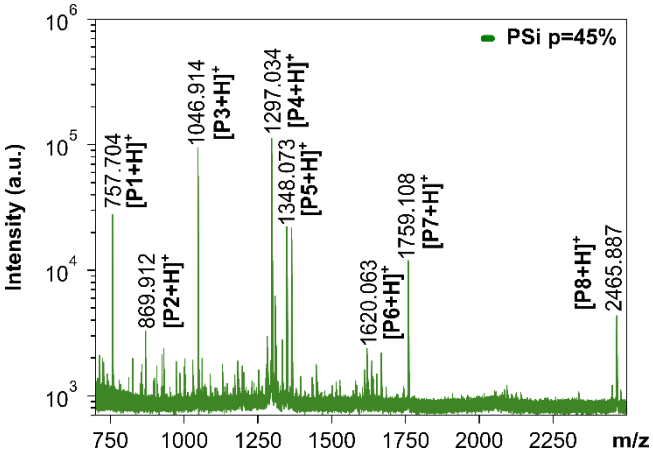

Figure 9 - Mass spectrum for peptide calibration standard II on a porous silicon surface of porosity 46%. Seven peptides, from a total of eight, from the mix were identified. Desorption/ionization of the highest mass peptide (Somatostatin 28, MW=3147.4719) was not observed.

CONCLUSION

In conclusion, this study proposes a methodical procedure for characterizing and optimizing LDI-MS by assessing the fragmentation of analytes.

The chosen model porous silicon substrates were synthetized by electrochemical etching of p-doped silicon wafers. The etching parameters were tuned to vary porosity while keeping a constant layer thickness of 700 – 1200 nm.

The effective temperature was employed as a metric to assess ion fragmentation, a critical factor in optimizing LDI-MS performance.

Our findings demonstrate that porous silicon substrates with porosities ranging from 40% to 60% exhibit optimal performance, characterized by lower effective temperature values indicating reduced fragmentation.

This trend was further corroborated through the analysis of N-Acetyl glucosamine, a carbohydrate, which reinforced the relationship between substrate porosity and effective temperature.

Extending the analysis to peptides, specifically peptide P14R and a peptide mixture (Peptide Calibration Standard II, Bruker), demonstrated that the optimized porous silicon (PSi) substrates effectively facilitated the desorption and ionization of peptides up to a maximum mass of *m/z* 2465, corresponding to ACTH clip 1-17. Regarding the observed fragments, further investigation is in progress to clarify the nature of the observed fragmentation pathways (thermal or radical-induced) in order to gain a deeper understanding of the LDI-MS mechanism on PSi.

While other factors, such as surface-analyte interactions, laser absorption, and substrate thermal conductivity, likely play a role in the desorption/ionization process, further investigations using advanced characterization techniques are necessary to fully understand their influence.

These results highlight the importance of substrate porosity in minimizing analyte fragmentation in LDI-MS applications. This optimization of PSi substrates holds significant potential for improving the sensitivity and accuracy of LDI-MS, paving the way for more precise and reliable analytical applications in various scientific fields.

ACKNOWLEDGEMENTS

This project was funded by Wallonie Recherche (SPW) in the framework of the Win4Doc program (CANARI project, Convention n° 2110248) and Incize srl.

The authors would like to acknowledge the support of the Centre National de la Recherche Scientifique (CNRS), the Université de Lille and of the Centrale de Micro Nano Fabrication (CMNF) at the Institut d'electronique, Microélectronique et Nanotechnologie (IEMN). Acknowledgements are also due to the Wallonia Infrastructure Nano Fabrication (WINFAB) and the Wallonia ELectronics & COmmunications Measurements (WELCOME) at the Université catholique de Louvain.

The authors would also like to acknowledge Dr. Christopher Kune for his aid with the DFT computations.

This work was also partly supported by the French RENATECH network.

Computational resources have been provided by the Consortium des Équipements de Calcul Intensif (CÉCI), funded by the Fonds de la Recherche Scientifique de Belgique (F.R.S.-FNRS) under Grant No. 2.5020.11 and by the Walloon Region.

REFERENCES

(1) Tanaka, K.; Waki, H.; Ido, Y.; Akita, S.; Yoshida, Y.; Yoshida, T.; Matsuo, T. Protein and Polymer Analyses up to *m/z* 100 000 by Laser Ionization Time-of-flight Mass Spectrometry. *Rapid Comm Mass Spectrometry* **1988**, *2* (8), 151–153. https://doi.org/10.1002/rcm.1290020802.

(2) Karas, Michael.; Hillenkamp, Franz. Laser Desorption Ionization of Proteins with Molecular Masses Exceeding 10,000 Daltons. *Anal. Chem.* **1988**, *60* (20), 2299–2301. https://doi.org/10.1021/ac00171a028.

(3) Wei, J.; Buriak, J. M.; Siuzdak, G. Desorption–Ionization Mass Spectrometry on Porous Silicon. *Nature* **1999**, *399* (6733), 243–246. https://doi.org/10.1038/20400.

(4) Yanes, O.; Woo, H.-K.; Northen, T. R.; Oppenheimer, S. R.; Shriver, L.; Apon, J.; Estrada, M. N.; Potchoiba, M. J.; Steenwyk, R.; Manchester, M.; Siuzdak, G. Nanostructure Initiator Mass Spectrometry: Tissue Imaging and Direct Biofluid Analysis. *Anal. Chem.* **2009**, *81* (8), 2969–2975. https://doi.org/10.1021/ac802576q.

(5) Palermo, A. Charting Metabolism Heterogeneity by Nanostructure Imaging Mass Spectrometry: From Biological Systems to Subcellular Functions. *J. Am. Soc. Mass Spectrom.* **2020**, *31* (12), 2392–2400. https://doi.org/10.1021/jasms.0c00204.

(6) Patti, G. J.; Shriver, L. P.; Wassif, C. A.; Woo, H. K.; Uritboonthai, W.; Apon, J.; Manchester, M.; Porter, F. D.; Siuzdak, G. Nanostructure-Initiator Mass Spectrometry (NIMS) Imaging of Brain Cholesterol Metabolites in Smith-Lemli-Opitz Syndrome. *Neuroscience* **2010**, *170* (3), 858–864. https://doi.org/10.1016/j.neuroscience.2010.07.038.

(7) Qu, X.; He, B.; Li, Z.; Jiang, X.; Liu, X.; Chen, X.; Chen, X.; Liang, X.; Jiang, Z.; Wu, J. Accurate Discrimination of Benign Biliary Diseases and Cholangiocarcinoma with Serum Multiomics Revealed by High-Throughput Nanoassisted Laser Desorption Ionization Mass Spectrometry. *J. Proteome Res.* **2023**, *22* (6), 1855–1867. https://doi.org/10.1021/acs.jproteome.2c00846.

(8) Zhu, Q.; Wang, Z.; Wang, Y.; Teng, F.; Du, J.; Dou, S.; Lu, N. Investigation of Surface Morphology on Ion Desorption in SALDI-MS on Tailored Silicon Nanopillar Arrays. *J. Phys. Chem. C* **2020**, *124* (4), 2450–2457. https://doi.org/10.1021/acs.jpcc.9b09520.

(9) Guinan, T.; Ronci, M.; Vasani, R.; Kobus, H.; Voelcker, N. H. Comparison of the Performance of Different Silicon-Based SALDI Substrates for Illicit Drug Detection. *Talanta* **2015**, *132*, 494–502. https://doi.org/10.1016/j.talanta.2014.09.040.

(10) Hosu, I. S.; Sobaszek, M.; Ficek, M.; Bogdanowicz, R.; Drobecq, H.; Boussekey, L.; Barras, A.; Melnyk, O.; Boukherroub, R.; Coffinier, Y. Carbon Nanowalls: A New Versatile Graphene Based Interface for the Laser Desorption/Ionization-Mass Spectrometry Detection of Small Compounds in Real Samples. *Nanoscale* **2017**, *9* (27), 9701–9715. https://doi.org/10.1039/C7NR01069A.

(11) Naito, Y.; Kotani, M.; Ohmura, T. A Novel Laser Desorption/Ionization Method Using through Hole Porous Alumina Membranes. *Rapid Comm Mass Spectrometry* **2018**, *32* (21), 1851–1858. https://doi.org/10.1002/rcm.8252.

(12) Wang, X.-N.; Tang, W.; Gordon, A.; Wang, H.-Y.; Xu, L.; Li, P.; Li, B. Porous TiO_2 Film Immobilized with Gold Nanoparticles for Dual-Polarity SALDI MS Detection and Imaging. *ACS Appl. Mater. Interfaces* **2020**, *12* (38), 42567–42575. https://doi.org/10.1021/acsami.0c12949.

(13) Abdelmaksoud, H. H.; Guinan, T. M.; Voelcker, N. H. Fabrication of Nanostructured Mesoporous Germanium for Application in Laser Desorption Ionization Mass Spectrometry. *ACS Appl. Mater. Interfaces* **2017**, *9* (6), 5092–5099. https://doi.org/10.1021/acsami.6b14362.

(14) Pan, X.-Y.; Chen, C.-H.; Chang, Y.-H.; Wang, D.-Y.; Lee, Y.-C.; Liou, C.-C.; Wang, Y.-X.; Hu, C.-C.; Kuo, T.-R. Osteoporosis Risk Assessment Using Multilayered Gold-Nanoparticle Thin Film via SALDI-MS Measurement. *Anal Bioanal Chem* **2019**, *411* (13), 2793–2802. https://doi.org/10.1007/s00216-019-01759-5.

(15) Iakab, S.-A.; Baquer, G.; Lafuente, M.; Pina, M. P.; Ramírez, J. L.; Ràfols, P.; Correig-Blanchar, X.; García-Altares, M. SALDI-MS and SERS Multimodal Imaging: One Nanostructured Substrate to Rule Them Both. *Anal. Chem.* **2022**, *94* (6), 2785–2793. https://doi.org/10.1021/acs.analchem.1c04118.

(16) Luo, G.; Chen, Y.; Daniels, H.; Dubrow, R.; Vertes, A. Internal Energy Transfer in Laser Desorption/Ionization from Silicon Nanowires. *J. Phys. Chem. B* **2006**, *110* (27), 13381–13386. https://doi.org/10.1021/jp0609582.

(17) De Pauw, E.; Pelzer, G.; Marien, J.; Natalis, P. Internal Energy Distribution of Ions Emitted in Secondary Ion Mass Spectrometry. In *Ion Formation from Organic Solids (IFOS III)*; Benninghoven, A., Ed.; Lotsch, H. K. V., Series Ed.; Springer Proceedings in Physics; Springer Berlin Heidelberg: Berlin, Heidelberg, 1986; Vol. 9, pp 103–108. https://doi.org/10.1007/978-3-642-82718-1_21.

(18) Vékey, K. Internal Energy Effects in Mass Spectrometry. *J. Mass Spectrom.* **1996**, *31* (5), 445–463. https://doi.org/10.1002/(SICI)1096-9888(199605)31:5<445::AID-JMS354>3.0.CO;2-G.

(19) Frisch, M. J.; Trucks, G. W.; Schlegel, H. B. Gaussian 16, Revision B.01, 2016.

(20) Segal, E.; Perelman, L. A.; Cunin, F.; Di Renzo, F.; Devoisselle, J. -M.; Li, Y. Y.; Sailor, M. J. Confinement of Thermoresponsive Hydrogels in Nanostructured Porous Silicon Dioxide Templates. *Adv Funct Materials* **2007**, *17* (7), 1153–1162. https://doi.org/10.1002/adfm.200601077.

(21) Röst, H. L.; Schmitt, U.; Aebersold, R.; Malmström, L. pyOpenMS: A Python-based Interface to the OpenMS

Mass-spectrometry Algorithm Library. *Proteomics* **2014**, *14* (1), 74–77. https://doi.org/10.1002/pmic.201300246.

(22) Gabelica, V.; De Pauw, E. Internal Energy and Fragmentation of Ions Produced in Electrospray Sources. *Mass Spectrometry Reviews* **2005**, *24* (4), 566–587. https://doi.org/10.1002/mas.20027.

(23) Diao, Y.; Harada, T.; Myerson, A. S.; Alan Hatton, T.; Trout, B. L. The Role of Nanopore Shape in Surface-Induced Crystallization. *Nature Mater* **2011**, *10* (11), 867–871. https://doi.org/10.1038/nmat3117.

(24) Lehmann, V. *Electrochemistry of Silicon: Instrumentation, Science, Materials and Applications*, 1st ed.; Wiley, 2002. https://doi.org/10.1002/3527600272.

(25) Erfantalab, S.; Parish, G.; Keating, A. Determination of Thermal Conductivity, Thermal Diffusivity and Specific Heat Capacity of Porous Silicon Thin Films Using the 3ω Method. *International Journal of Heat and Mass Transfer* **2022**, *184*, 122346. https://doi.org/10.1016/j.ijheatmasstransfer.2021.122346.

(26) Demeure, K.; Gabelica, V.; De Pauw, E. A. New Advances in the Understanding of the In-Source Decay Fragmentation of Peptides in MALDI-TOF-MS. *J. Am. Soc. Mass Spectrom.* **2010**, *21* (11), 1906–1917. https://doi.org/10.1016/j.jasms.2010.07.009.

(27) Asakawa, D. Principles of Hydrogen Radical Mediated Peptide/Protein Fragmentation during Matrix-assisted Laser Desorption/Ionization Mass Spectrometry. *Mass Spectrometry Reviews* **2016**, *35* (4), 535–556. https://doi.org/10.1002/mas.21444.